AIAA JOURNAL
Vol. 37, No. 10, October 1999

Hemisphere Cylinder at Incidence at Intermediate to High Reynolds Numbers

Ngoc T. Hoang,* Othon K. Rediniotis,† and Demetri P. Telionis‡
Virginia Polytechnic Institute and State University, Blacksburg, Virginia 24061-0219

Careful documentation of the development of leeward vortices and separation bubbles over a hemisphere–cylinder body at intermediate to high Reynolds numbers is presented. Flow visualization, static pressure measurements, seven-hole probe anemometry, and laser Doppler velocimetry were employed to provide a complete picture of the flow at angles of attack of 0, 10, 20, and 30 deg. Composites of skin-friction lines and static pressure data are presented. Comparisons are made of the results obtained by a seven-hole probe and a fiber-optic laser Doppler velocimetry probe.

Introduction

In the past few years, great gains have been made in understanding and in calculating the intricate structures of complex fluid flows. We can now calculate with great accuracy transonic or supersonic flows, but problems involving three-dimensional separating flows still pose considerable difficulties. The situation is exacerbated by our inability to predict transition to turbulence, a feature of the flow that greatly influences separation in three dimensions. Moreover, it is hard to capture turbulent free shear layers that undulate in space.

Three-dimensional flows were explored both experimentally and numerically, with emphasis first on the development of laminar boundary layers in three dimensions.[1–3] Interest then shifted to the characteristics of separation in three dimensions. Our understanding of this feature of the flow was considerably enhanced with studies of the topography of skin-friction lines. Earlier descriptions of Maskell[4] and Lighthill[5] were revisited,[6–9] and the significance of the singular behavior of these patterns was intimately connected with flows over specific, well-defined geometries. Most of the work at that time was concentrated on the flow over a prolate spheroid. Work was extended to study the structure of three-dimensional turbulent boundary layers over this configuration.[10–13] New developments in experimental methods then allowed the exploration of the separated flow above the surface of the body.[13–16]

A feature of the flow that is unexpected to students of two-dimensional problems is that the flow from upstream approaches the separation line from both its sides. The concept, therefore, that the line of separation separates the attached flow from the wake is no longer meaningful. This type of three-dimensional separation is known as open separation.[3] Of particular interest here is that the flow approaching the line of separation from the windward side could be laminar, while the flow on the other side could be turbulent.[10,11] (The line of separation is inclined with respect to the freestream. It is, therefore, still meaningful to refer to its windward and leeward sides.) Costis and Telionis[14] and Costis et al.[15] pointed out that, on the leeside, the boundary layer involves substantial crossflow and heavily inflectional profiles that could not sustain large-Reynolds-number laminar flows.

The simplicity of the flow separation over prolate spheroids with aspect ratios larger than 4 is that the separation lines emerge over the surface of the body without the upstream appearance of any singularities in the skin-friction line patterns. This is not the case for flows over blunt-nosed bodies such as the hemisphere–cylinder studied here.[14] For such bodies, nose separation rings may develop, as well as tornadolike vortex structures that appear rooted on the surface of the body.[17,18] Such vortices are also termed horn vortices. Open separation originates from the roots of horn vortices.

Very careful and detailed experimental studies of turbulent separating flows over the $\frac{6}{1}$ prolate spheroid appeared recently.[12,13] Barberis and Molton[12] employed laser anemometry and three-hole probes to measure turbulent boundary-layer properties such as mean profiles and Reynolds stresses for angles of attack up to 20 deg. Their laser Doppler velocimetry (LDV) arrangement was limited to meridian planes, but they also provided extensive pressure distributions. They concluded that, for a 20-deg incidence, separation had no appreciable effects on surface pressure. Chesnakas and Simpson[13] designed and constructed a fiber-optic LDV probe that permitted them to obtain detailed measurements within the boundary layer and obtained profiles of quantities such as turbulent kinetic energy and turbulence anisotropy. They indicated that the line of separation is characterized by a minimum of wall shear but demonstrated that none of the diagnostic techniques is completely reliable in revealing separation topology and indicated that the surface flow visualization may still be the simplest and at least equally reliable method to map out the line of separation. In the present paper, we present composite figures overlaying digitized surface flow data with surface pressure distributions. Moreover, we extend the study to an angle of attack of 30 deg and explore the outer flow much farther away from the wall, thus capturing the vortical structures in their entirety. Pressure distributions over the hemisphere–cylinder were reported by Meade and Schiff,[9] but these data were obtained in supersonic flows.

The prolate spheroid leads the flow very smoothly toward the separation lines.[12,13] There are no other separating flow structures upstream. The flow over the hemisphere–cylinder under consideration here displays, at intermediate Reynolds numbers, separation bubbles that terminate along horn vortices. These upstream structures probably influence the character of the separating flow farther downstream. The exploration of these structures and their relationship to open separation lines and wake vortices is the goal of the present paper.

Experimental Setup

Experiments were conducted in the 1.83×1.83 m (6×6 ft) Virginia Polytechnic Institute and State University Stability Wind Tunnel. Speeds over 90 m/s can be achieved in this facility with excellent uniformity of flow. The turbulence level is below 0.07%. The tunnel is equipped with struts and stings that can securely support large, heavy models with minimum obstruction to the flow. The aim is to study this three-dimensional flow at intermediate to high Reynolds numbers in an extremely quiet environment and without artificially fixing the location of transition.

Received 13 March 1998; revision received 10 February 1999; accepted for publication 15 March 1999.

*Graduate Research Assistant, Department of Engineering Science and Mechanics; currently President, NAL Research Corp., 8708 Sudley Road, Manassas, VA 20110. Member AIAA.

†Graduate Research Assistant, Department of Engineering Science and Mechanics; currently Assistant Professor, Aerospace Department, Texas A&M University, College Station, TX 77843. Member AIAA.

‡F. J. Maher Professor, Department of Engineering Science and Mechanics. Associate Fellow AIAA.

To test the wall effects, static pressure distributions on the test-section wall were obtained with the hemisphere–cylinder model at $\alpha = -20, -10, 10$, and 20 deg. Along the bottom wall of the test section at a spacing of 1.25 cm, 24 1.16-mm-diam orifices were drilled. These experiments were conducted at a model Reynolds number of 2.9×10^5. Hoang[19] has shown that the deviations in the tunnel wall pressure distribution with the model at various angles of attack and without the model were at most equal to $\Delta C_p = \pm 0.003$. Thus, it can be safely assumed that the blockage effect introduced by the presence of the body in the wind tunnel is negligible.

A 19.06-cm-diam hemisphere–cylinder was machined out of aluminum in three separate pieces: a hemispherical nose and two cylindrical afterbody sections (Fig. 1a). The first was on loan from the Fluid Dynamic Branch of NASA Langley Research Center. The model was hollow to provide space for instrumentation. Two 3.18-cm slots were cut axially along the afterbody portion to allow the LDV laser beams to be directed from the inside of the model as shown in Fig. 1a. The slots were fitted with windows of different materials including plexiglass and glass. However, it was discovered that high-quality acrylic was best suited for the reduction of flare. The model was turned with the windows, so that a flat area with a width of only 2.29 cm was left, corresponding to a radial defect, i.e., a deviation from the circular arc of 0.013 mm, i.e., about 0.013% geometrical error. Surface flow visualization did not indicate any effect on the flow due to the flatness of the window. To reduce the chance that such disturbances could occur, it was always attempted to place the windows underneath the separated flow or on the other side of the measurements.

The system of coordinates is shown in Fig. 1b. The Cartesian system of coordinates ℓ, y, z has its origin at the point where the axis of symmetry penetrates the hemisphere. Distances along meridional planes and along the surface of the body are denoted by x. Static pressure was measured by pressure taps connected to a pressure scanner. The model had 94 pressure orifices, each 0.8-mm in diameter, along the x direction at a constant ϕ. The orifices were spaced closer to each other near the nose than the afterbody of the cylinder to provide reliable measurements across the separation bubble. The model was manually rolled in the wind tunnel about its axis of symmetry to measure pressure at various cross-sectional stations. Static pressure coefficients on the surface of the hemisphere–cylinder were obtained at $\alpha = 0$, 10, 20, and 30 deg for $Re = 2.9 \times 10^5$ and 4.2×10^5 for $\phi = 0$–180 deg in 20-deg increments. For $\alpha = 0$, 10, and 20 deg, pressure data were also taken along the x axis at $\phi = 180$ deg and at five different Reynolds numbers. Flow visualizations indicated that the flow is symmetric about the geometrical plane of symmetry. For this reason, pressure data were obtained only along the starboard side of the model. Previously, we have demonstrated[18] that the flow over blunt-nosed bodies, such as the current model, does not display asymmetric wakes until much higher angles of attack and only if triggered by a physical disturbance near the nose.

For axisymmetric configurations, the use of LDVs with beams directed through wind-tunnel windows is inconvenient. For such configurations, difficulties are encountered in accessing all of the regions of interest. More importantly, it is hard to position the measuring volume accurately with respect to the model. These problems can be solved by directing the beams from inside the model. This can be accomplished today with a fiber-optic LDV probe. We used a probe in which the sending and receiving optics are packaged by TSI, Inc., in a small cylinder about 1.25 cm in diameter and 6 cm in length. The current authors have presented data obtained in this way earlier.[20] More recently, Chesnakas and Simpson[13] designed and constructed a fiber-optic probe that permitted them to obtain measurements much closer to the surface of their model than the TSI probe would.

The TSI fiber-optic probe was mounted inside the model on a linear traversing table. The beams were directed through the windows, perpendicular to the surface of the model, as shown in Fig. 2. Rotation of the entire model facilitated positioning along a parallel circle of a polar coordinate system. To traverse the measuring volume parallel and perpendicular to the axis of the model, a traversing system was constructed, which is shown inside the model in Fig. 2. Mirrors were used to turn the beams normal to the model wall. A CXT 29-35 Compumotor stepping motor was employed in two optional configurations. In one option, the LDV probe was displaced while the mirror was kept fixed, thus facilitating displacement of the measuring volume in a direction normal to the axis of the model. In the second option, probe and mirror were displaced together. This allowed the measuring volume to be traversed along a direction parallel to the axis of the model. The error in positioning of the measuring volume due to the refraction effect was eliminated by careful positioning calibration.

Measurements were also obtained with a seven-hole probe constructed and calibrated for this project.[19] A traversing table was mounted on the sting support behind the model. Unlike the LDV

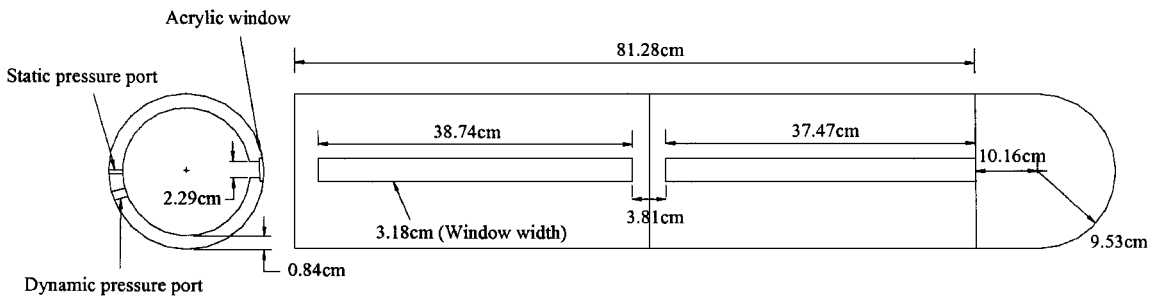

Fig. 1a Model.

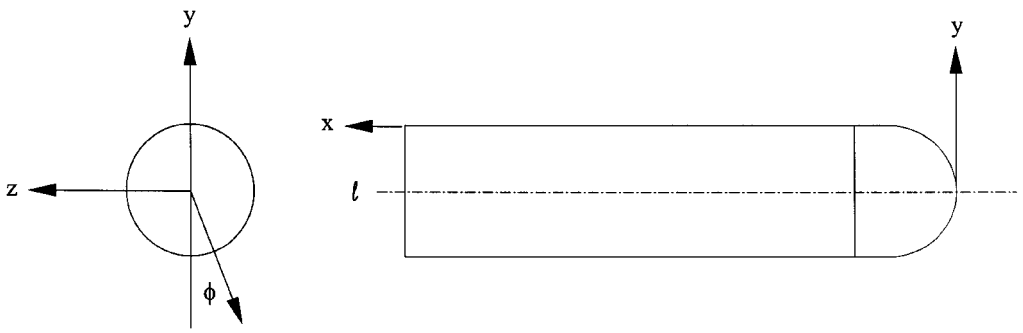

Fig. 1b Coordinate system.

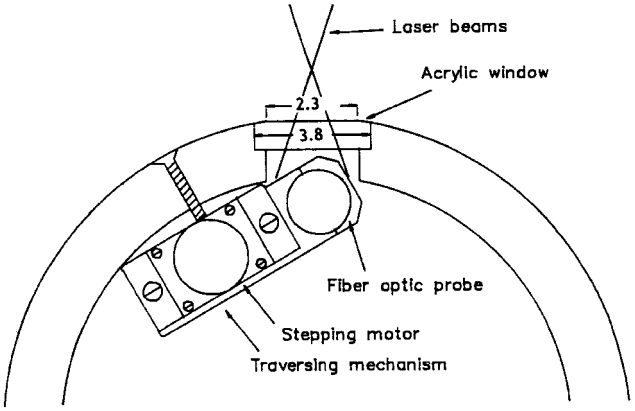

Fig. 2 Cross section of the traversing mechanism shown inside the model.

setup, rotation of the entire traversing mechanism instead of the model facilitated positioning along a parallel circle of a polar coordinate system. To traverse along the x direction, the traversing mechanism could be placed at different locations along the mounting sting. A stepping motor was employed to displace the seven-hole probe in the direction normal to the surface of the model. The entire assembly could be positioned at different angles of attack by independent rotations of the vertical lead screws of the model mount.

The velocity field over the hemisphere–cylinder model was documented via seven-hole probe and LDV measurements at six different cross-sectional stations, $x/R = 5.8$, 6.1, 8.1, 8.4, 9.7, and 10.0, and two angles of attack, $\alpha = 20$ and 30 deg. The fiber-optic LDV system allows the simultaneous measurement of only two velocity components, whereas three velocity components can be obtained with the seven-hole probe. In some regions of the flow, considerable differences between readings of the two instruments were found. These are discussed later in this paper.

To visualize the flow, the classical method of painting the model with a mixture of titanium oxide was used. Skin-friction line visualizations were obtained at two different free-stream velocities, $U_\infty = 22.5$ m/s (74 ft/s) and 32.9 m/s (108 ft/s), and angles of attack $\alpha = 0$, 20, and 30 deg. The corresponding Reynolds numbers were 2.9×10^5 and 4.2×10^5, respectively. Photographs were taken at $\phi = 90$ deg (side view) and 180 deg (leeward view). Side views of the flow visualization photographs were digitized for $\alpha = 20$ and 30 deg.

A DATATAB graphic digitizer was used to convert the flow visualizations to numerical data. The operational system consists of four major units: a graphic table, a controller, a 16-digit keypad, and an output device. The graphic table has an imbedded electronic grid that can be read by the controller via a keypad. Data are transmitted to the computer in the form of two five-digit numbers. When the keypad is placed on the graphic table surface, the X–Y positions of the cross hair on the keypad with respect to the table are displayed. As the keypad moves about the surface of the table, the X–Y positions may be recorded with a resolution and repeatability of 0.002 cm.

The pressure transducers were calibrated every few hours. A five-point calibration was performed that accounted for transducer nonlinearities and thermal drifts. Taking into account reference manometer uncertainty and A/D conversion uncertainty, this yielded a pressure measurement worst-case error of 0.025 torr or 0.033 cm in H_2O, which meant that there was a 99.5% probability that the pressure measurement error was smaller or equal to 0.025 torr. Errors in angular positioning were negligible. The resolution of the cone and roll positioning stepper motors (1.8 and 0.09 deg) should not be confused with their positioning precision, which is on the order of arc seconds. Bias errors due to probe sting deflection were also negligible at the speeds of calibration and for the specific structural design of the probe. The uncertainty in the measurement of the seven-hole probe pressures propagates through the probe data-reduction routines to the final predictions.[19,21] To evaluate the total prediction uncertainty (combined pressure measurement and data-reduction uncertainty) the jitter approach[22] was followed. The overall uncertainty was estimated as the rms of individual uncertainties, and it was found to be about 1 deg in cone angle, 1.2 deg in roll angle, and 1.5% in velocity magnitude. However, in regions of large shear, these estimates are inadequate and well below the actual error. More discussion on this issue follows.

Using a similar approach, the uncertainty of the fiber-optic LDV probe can be calculated. The uncertainties for each independent variable were assumed to be 0.01 deg for half-angle between the laser beams, 0.56 kHz for the IFA550 signal processor, and 0.2 kHz for the frequency shifter. The largest uncertainty in both velocity components was found to be 0.058 m/s. Again, it is anticipated that in regions of high shear, where seeding is difficult, the error may be higher.

Results and Discussion

Flow Visualization and Digitization

At 0-deg angle of attack and $Re = 2.9 \times 10^5$, a laminar separation bubble develops near the juncture of the hemisphere and the cylinder, similar to the flow pattern at low Reynolds numbers. This bubble is closed and forms two rings around the body, a separation ring at $x/R = 1.55$ and a reattachment ring at $x/R = 1.70$ (not shown here due to lack of space). The length of the separation bubble in the axial direction is much smaller here than at low-Reynolds-number flows.[18] The separation bubble was also detected by liquid-crystal tests, designed for skin-friction measurements. This part of the investigation was carried out in cooperation with with G. S. Jones of NASA Langley Research Center. Although not shown here due to poor quality of the photographs, liquid-crystal solution visualizations indicate a region of very low skin-friction magnitude across the separation bubble and very large magnitudes after reattachment.

Flow visualization data are available[19] for $\alpha = 10$, 20, and 30 deg and Reynolds numbers of $Re = 2.9 \times 10^5$ and 4.2×10^5. Here we present data only for $\alpha = 20$ deg and $Re = 2.9 \times 10^5$. Figures 3a and 3b show two different views, $\phi = 180$ and 90 deg. Such data were digitized to generate skin-friction lines, which are presented here in Figs. 4 and 5 for $\alpha = 20$ and 30 deg. In these figures, we also display pressure contours, which will be discussed later.

For $\alpha = 10$ deg and $Re = 2.9 \times 10^5$, the separation bubble disappears on the windside and is confined to the leeside of the model at $x/R = 1.5$ and from $\phi = -90$ to 90 deg. The width of the bubble remains nearly constant in the meridional direction. The existence of horn vortices[17,18] cannot be confirmed with certainty based on the flow visualization photographs. However, during the experiment,

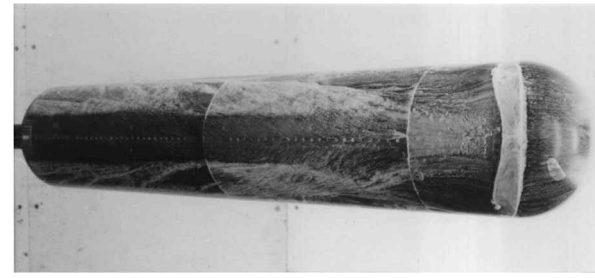

a) $\phi = 180$ deg

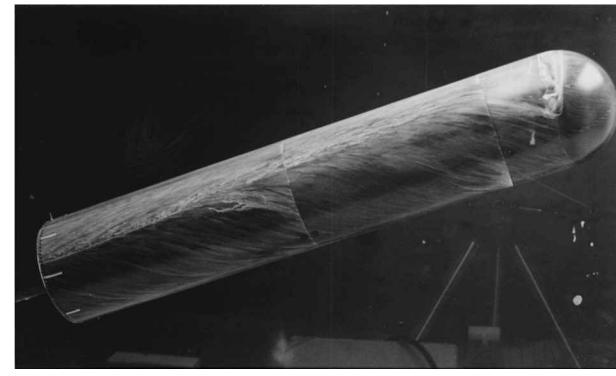

b) $\phi = 90$ deg

Fig. 3 Surface flow visualization at $\alpha = 20$ deg and $Re = 2.9 \times 10^5$.

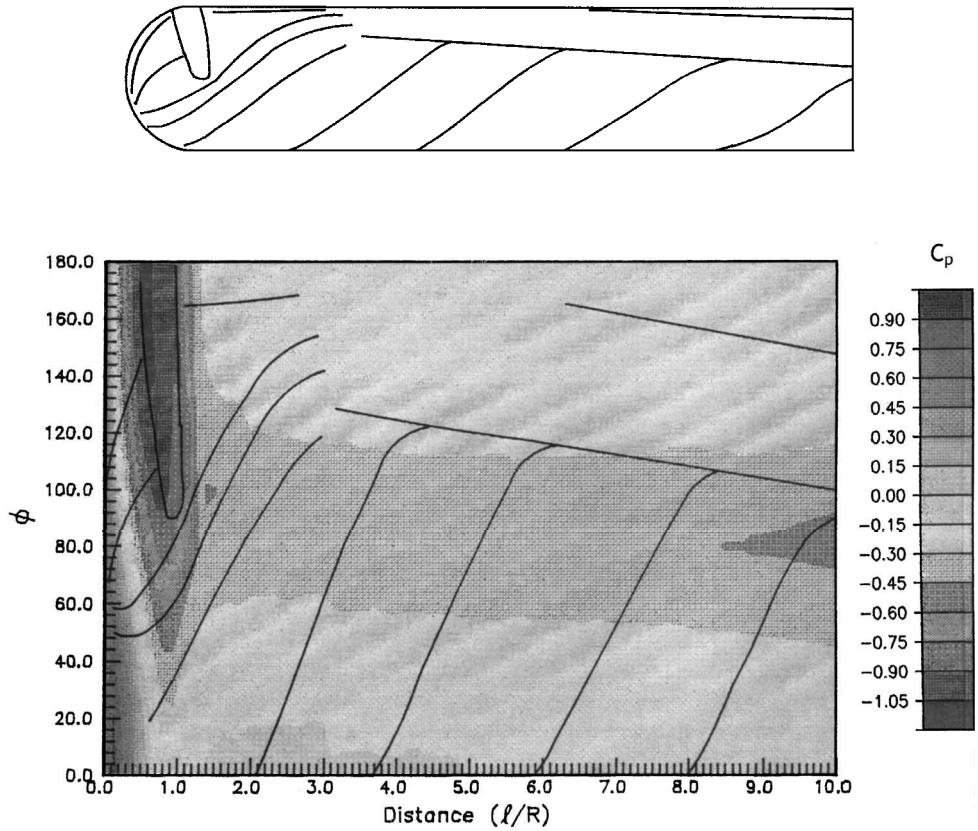

Fig. 4 Pressure coefficient contours and digitized skin-friction patterns on a hemisphere–cylinder at $\alpha = 20$ deg and $Re = 2.9 \times 10^5$.

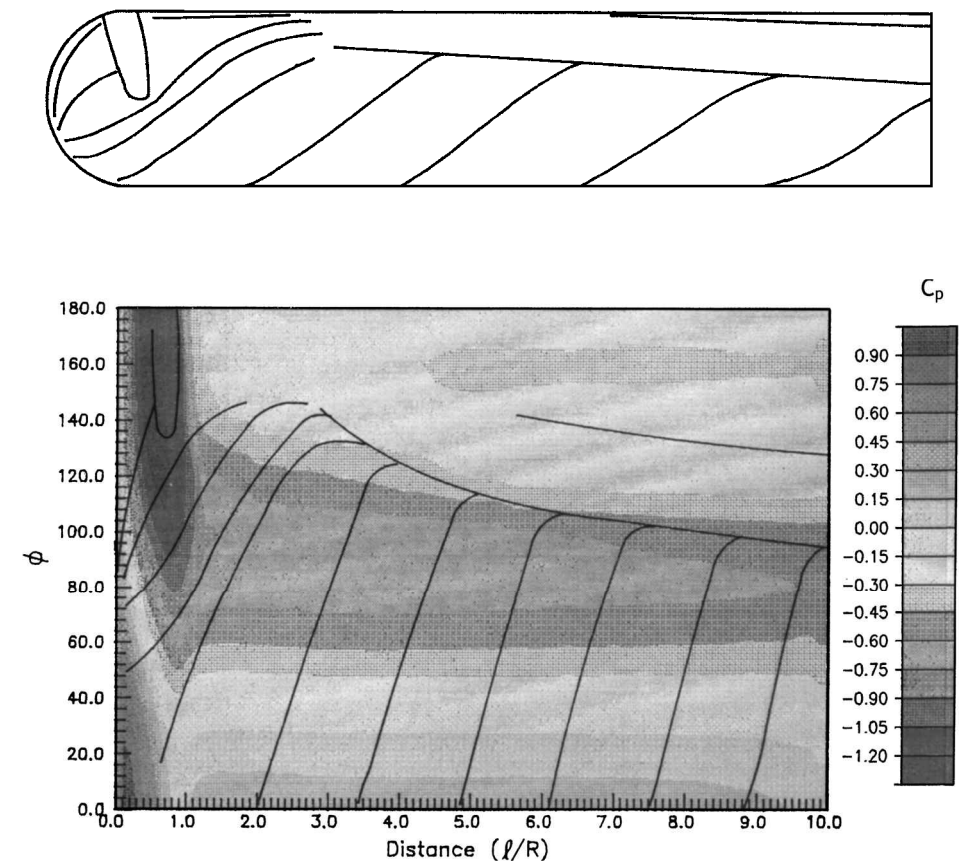

Fig. 5 Pressure coefficient contours and digitized skin-friction patterns on a hemisphere–cylinder at $\alpha = 30$ deg and $Re = 4.2 \times 10^5$.

there seemed to be a heavy amount of titanium dioxide mixture swirling around the region of $\phi = 90$ deg and $x/R = 1.5$, as may be seen in Fig. 3. The wind tunnel had to be kept running while photographs were taken to prevent flow visualization mixture accumulation near the nose from running. Thus, it appears that two very weak horn vortices do exist at this Reynolds number. The authors[18] have earlier reported that at the same angle of attack, $\alpha = 20$ deg, and low Reynolds number the horn vortices seem to reach their maximum size and strength.

Farther downstream, the flow develops an open separation region, namely, merging of the skin-friction lines as shown in Fig. 3. This can be best detected by the digitized skin-friction lines shown in Fig. 4. A primary separation line appears, from $\phi = 130$ deg, $\ell/R = 3$ to $\phi = 100$ deg, $\ell/R = 10$, as an envelope of skin-friction lines. The secondary separation line stretches along the cylindrical afterbody from $\phi = 165$ deg, $\ell/R = 5$ to $\phi = 150$ deg, $\ell/R = 10$. Free shear layers are rooted along primary and secondary separation lines and lift off to form two shear layers. These layers interact with each other and roll into a large-scale vortex. The same phenomenon occurs on the other half of the model as well.

At $\alpha = 30$ deg and for low-Reynolds-number flows, an order of magnitude lower than under consideration here, the leeward vortices and the separation bubble merge together to form a single separated region known as the horseshoe vortex.[17,18] The flow displays a closed-type separation. The opposite is observed here for high-Reynolds-number flows. There is a large space between the leeward vortices and the separation bubble, and the flow patterns indicate open separation. The horn vortices completely vanish.

Axial pressure distributions were obtained at zero incidence along two meridional planes, $\phi = 0$ and 90 deg for $Re = 2.9 \times 10^5$. The data along $\phi = 0$ and 90 deg collapse (not shown here), confirming that the flow is symmetric about the model axis and that the freestream contains no angularity and no deviations from uniform flow.[19] A rather significant finding is the influence of the Reynolds number. This is most clearly demonstrated in the axial pressure distributions shown in Fig. 6. In this figure, data obtained over a much smaller model are also included. Flat horizontal sections of the pressure distribution are clear indications of separated flow. It is apparent that, for low Reynolds numbers, the pressure does not drop as much ($C_p = -0.4$) and that the separation bubble is much wider in the x direction. The flow remains laminar downstream of the separation bubble. This was also confirmed by flow visualization photographs presented in Fig. 3. For higher Reynolds numbers, with a much smaller separation bubble, the pressure over the attached region drops to a lower value ($C_p = -0.75$), approaching close to the ideal distribution. This is typical behavior of transition followed by turbulent reattachment, which should be expected at Reynolds numbers over 10^5. The boundary layer is turbulent downstream of the separation bubble. The pressure distribution calculated for ideal flow over a sphere is shown in Fig. 6 for comparison.

A considerable amount of data were obtained[19] that cannot be displayed here due to lack of space, but a brief description of the message they convey follows. Axial pressure data obtained for $\alpha = 0$ deg and at a sequence of intermediate to high Reynolds numbers indicate that near the separation bubble, a flat region displayed by the pressure curve progressively disappears with increasing Reynolds number (Mach number). In fact, at $Re = 1.10 \times 10^6$ ($M_\infty = 0.26$), the flat region can no longer be detected. These pressure variations capture the decrease of the extent of the separation bubble until its disappearance.

For the model at incidence, $\alpha = 10$ deg, at a Reynolds number of 4.2×10^5, all of the pressure data display narrow flat regions of constant pressure, indicating the existence of a separation bubble at $1.5 < x < 1.8$. Steep pressure gradients are isolated in a small region in front of the separation bubble, from $x/R = 0.0$ to 0.6. For x/R greater than 2.0, the pressure coefficients remain virtually unaffected by the parameter x/R. Hoang[19] presents axial pressure coefficients along a meridional plane, $\phi = 180$ deg, for seven different Reynolds numbers. Similar to the 0-deg incidence case, the separation bubble decreases in size with increasing Reynolds number and eventually vanishes at $Re = 1.10 \times 10^6$.

For $\alpha = 20$ deg and $Re = 2.9 \times 10^5$, axial pressure plots are shown in Fig. 7. To distinguish these curves, a constant ordinate value was added as indicated on the right side of Fig. 7. A peculiar behavior is revealed by the Fig. 7 plots; the pressure coefficient within the separation bubble, along $\phi = 180$ and 160 deg, drops to a minimum instead of remaining constant. However, the nearly flat regions appear along $100 < \phi < 140$ deg, indicating that the separation bubble is confined to the top of the model's nose. Pressure contours obtained in this way are shown in Fig. 4, superimposed on the digitized skin-friction patterns. It is now observed that the separation bubble locates in an area of minimum pressure coefficients. Axial pressure distributions and a composite of pressure coefficient contours at $\alpha = 20$ deg and $Re = 4.2 \times 10^5$ (not shown here) indicate that the length of the separation bubble is decreased slightly.

The pressure distributions for $\alpha = 20$ deg (Figs. 4 and 7) indicate three very distinct patterns. The first is found in the leading region of the model. In this region, the reduced pressure is high on the windward side and continuously decreases toward $\phi = 180$ deg. This behavior resembles two-dimensional lifting surfaces, whereby suction conditions are generated on the leeside of the body. The transition from the first to the second region is somewhat abrupt and occurs between $x/R = 1.6$ and 1.8. In the second region, the

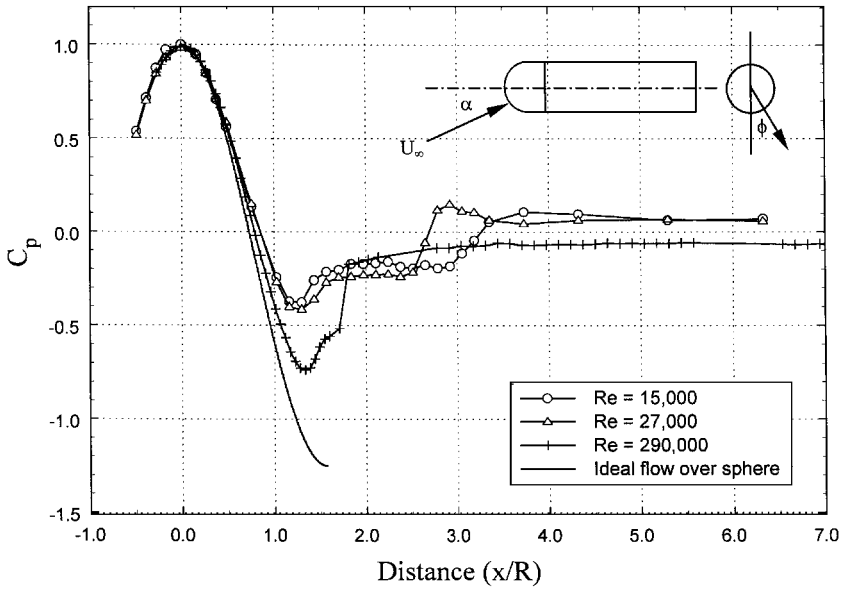

Fig. 6 Axial pressure distributions on a hemisphere–cylinder at $\alpha = 0$ deg and three different Reynolds numbers.

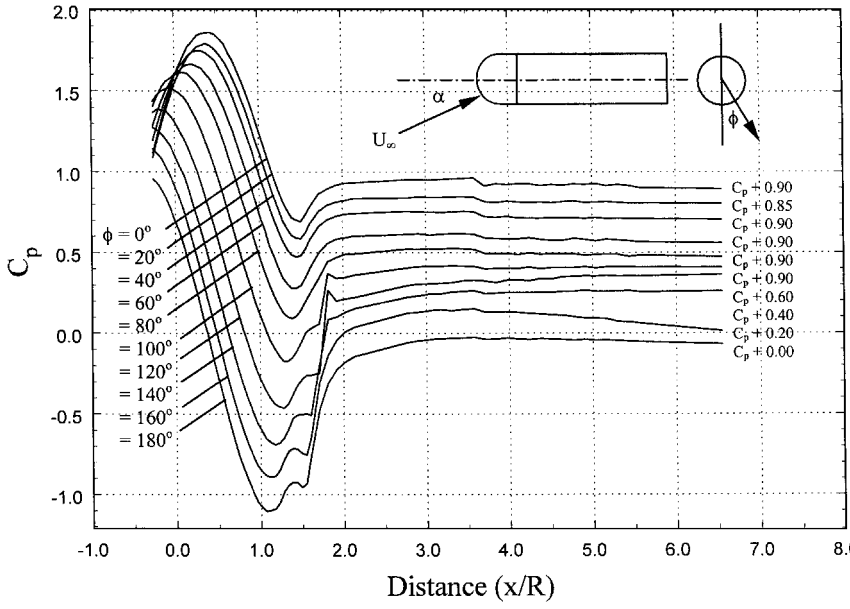

Fig. 7 Axial pressure distributions on a hemisphere–cylinder at $\alpha = 20$ deg and $Re = 2.9 \times 10^5$ with added constants.

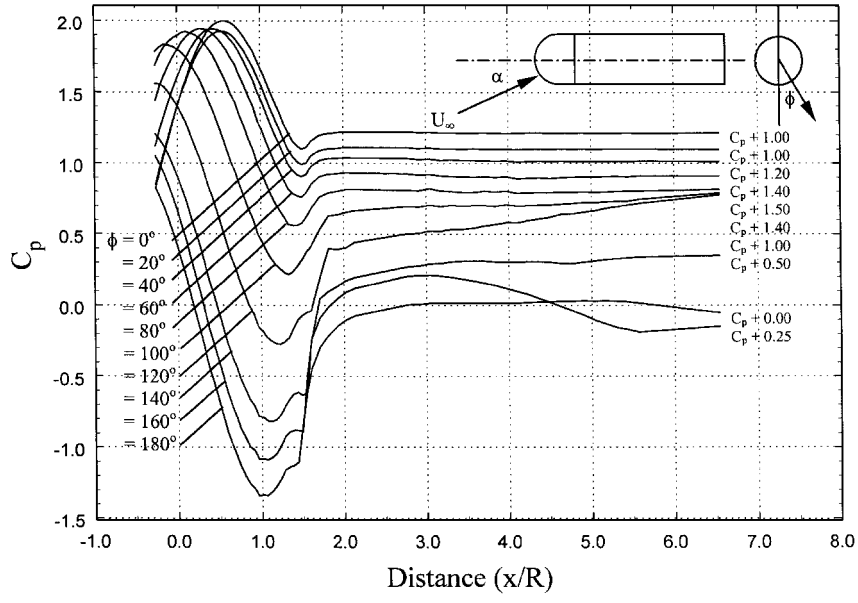

Fig. 8 Axial pressure distributions on a hemisphere–cylinder at $\alpha = 30$ deg and $Re = 4.2 \times 10^5$ with added constants.

pressure distribution is nearly symmetric about $\phi = 90$ deg, which is similar to two-dimensional ideal flow over a circular cylinder, i.e., flow without separation. The first two regions are nearly inviscid. No significant thickening of the boundary layer develops, even though the onset of open separation is clearly indicated in the second region, as displayed by the convergence of the skin-friction lines. The effect of viscosity becomes significant only in the third region, where the imprint of a separated vortex appears in the form of a dip in the pressure distribution, as shown in Fig. 5.

Axial pressure distributions obtained along the leeward meridional at $\alpha = 20$ deg for a Reynolds number sweep indicate that the separation bubble is once again reduced in length with increasing Reynolds number, although it does not completely disappear. It is interesting that the influence of the Reynolds number on the surface pressure at high-Reynolds-number flows is apparent, although somewhat localized in the region of the separation bubble. Figure 8 shows the axial pressure distributions for $Re = 4.2 \times 10^5$ at $\alpha = 30$ deg. The separation bubble can still be observed in these pressure curves but is isolated to the small region on the top of the model near $x/R = 1.5$.

Velocity Measurements

Velocity was measured first by a seven-hole probe. To evaluate probe interference with the flow, static pressure distributions of a hemisphere–cylinder were obtained along a meridional plane with the seven-hole probe mounted immediately above the solid surface at different radial locations. Pressures along the same line were also measured without the presence of the probe. Hoang[19] presents detailed data. The basic finding is that if the probe is placed as near as 1.3 probe diameters to the surface, the pressure coefficient can be affected by 70%, but if this distance is increased to 3, the influence is less than 5%. For $\alpha = 30$ deg and $Re = 1.5 \times 10^5$, the probe was positioned outside and inside the vortex core at $\phi = 90$ and 170 deg, respectively. The probe had a noticeable effect on the surface pressure data (7% influence) only when located at less than 2 probe diameters away from the center of the core.

The crossplane velocity vectors obtained with a seven-hole probe at six different axial stations are shown in Fig. 9. These frames show the development of the flow in crossflow planes along the body. The experiments were conducted at an angle of attack $\alpha = 20$ deg and $Re = 1.5 \times 10^5$. At $x/R = 5.8$, the leeward vortex is small but clearly visible with the core at approximately

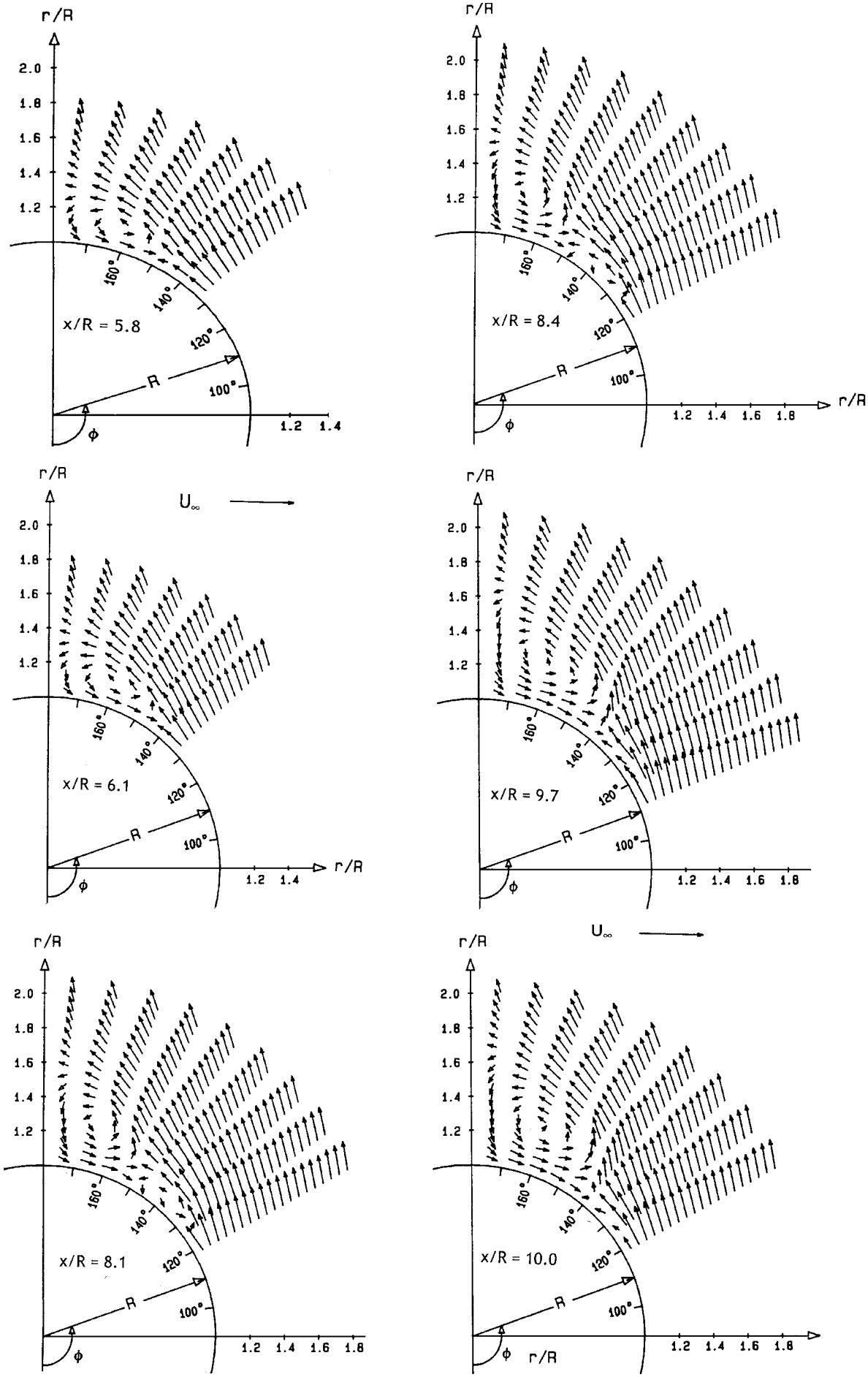

Fig. 9 Seven-hole probe velocity vector fields along a normal plane at $x/R = 5.8$, $\alpha = 20$ deg, and $Re = 1.5 \times 10^5$.

$\phi = 165$ deg. Separation occurs near $\phi = 145$ deg and then moves toward $\phi = 130$ deg at $x/R = 10.0$. The vortex appears to grow both in size and strength with downstream distance but still forms well beyond $\phi = 90$ deg. This is perhaps because, for $\alpha = 20$ deg, the axial component of the motion is quite dominant and the crossflow deviates substantially from the two-dimensional case. At $x/R = 8.1$ and 8.4, the primary and secondary separation points are found at $\phi = 120$ and 145 deg, respectively. The core of the leeward vortex remains at $\phi = 165$ deg. There exists another smaller vortex (secondary vortex) in the region between the primary and secondary separation points. The sense of rotation of this vortex is the same with the dominant leeward vortex. The dominant vortex will be referred in the sequel as the primary vortex.

Velocity data obtained with a fiber-optic LDV probe and a seven-hole probe under the same conditions are plotted in Figs. 10–12. In both Figs. 10 and 11, constants of 0.5 and 1.0 were added to both LDV and seven-hole probe curves at $\phi = 154$ and 161 deg, respectively. In Fig. 12, constants of 0.5 and 1.6 were added to both LDV and seven-hole probe curves at $\phi = 140$ and 161 deg. The purpose of Figs. 10–12 is to compare the accuracy of the velocity data taken with the seven-hole probe. At $x/R = 5.8$, data for the circumferential component shown in Fig. 10 indicate a good agreement away from the vortex and some deviation within the vortex. Apparently, the seven-hole probe registers consistently lower values within the recirculating region. There is little influence in the axial component (Fig. 11), except again within the vortex, where the values obtained by the seven-hole probe are lower. At this station, the ratio of the size of the probe to the size of the vortex is quite large. The probe generates a global interference to the flow. Large errors are registered in the circumferential components within the vortex. Differences as large as 46% are observed. Insertion of the probe at locations where the vortex is still small and weak may distort the flow and induce some sort of vortex breakdown.

At $x/R = 9.7$ (Fig. 12), the errors in both axial and circumferential components of velocity are confined to the neighborhood of the shear layer near the point of separation, $\phi = 140$ deg. The probe has little effect on the flow within the vortex because the wake has already developed into a strong leeward vortex. For this case, errors involved in seven-hole probe data are probably due to large local velocity gradients in a plane parallel to the axis of the seven-hole

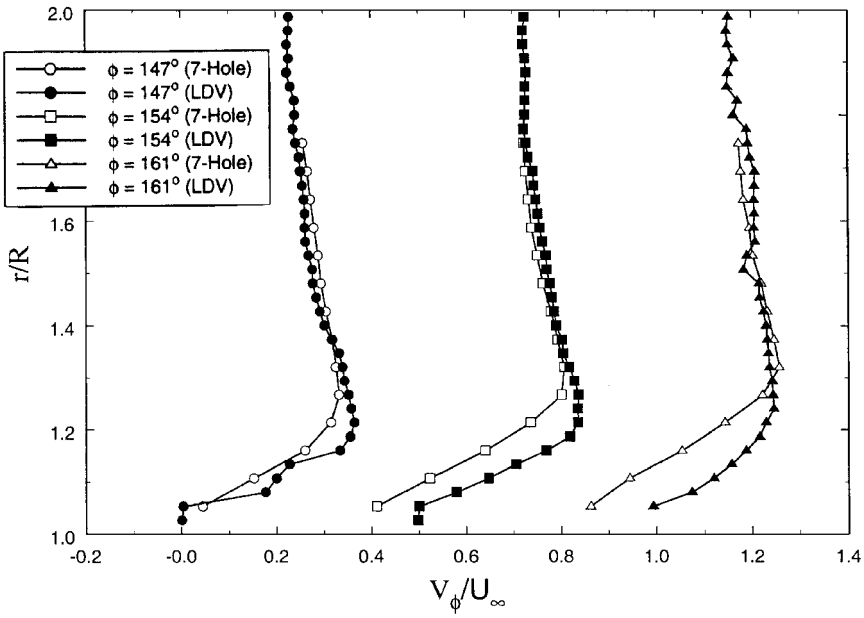

Fig. 10 LDV and seven-hole probe circumferential velocity profiles at $x/R = 5.8$, $\alpha = 20$ deg.

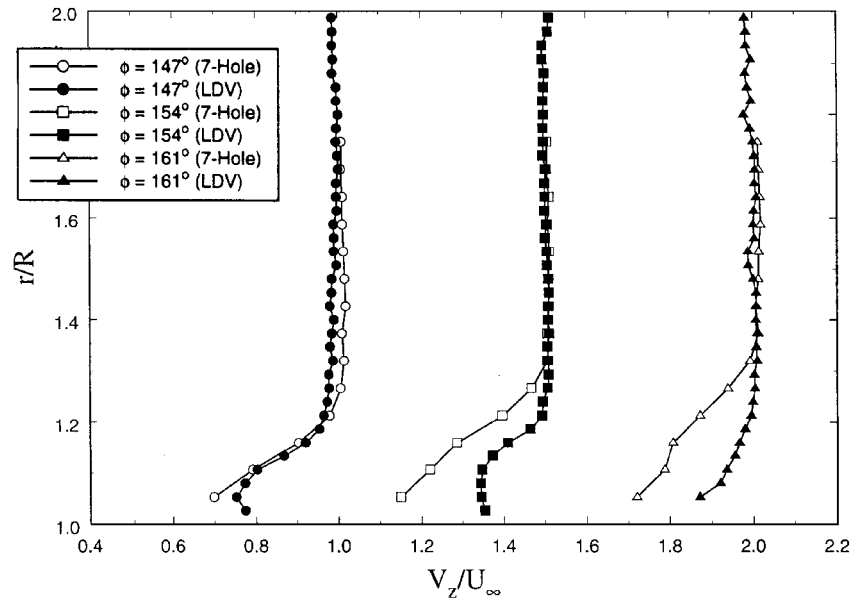

Fig. 11 LDV and seven-hole probe axial velocity profiles at $x/R = 5.8$, $\alpha = 20$ deg.

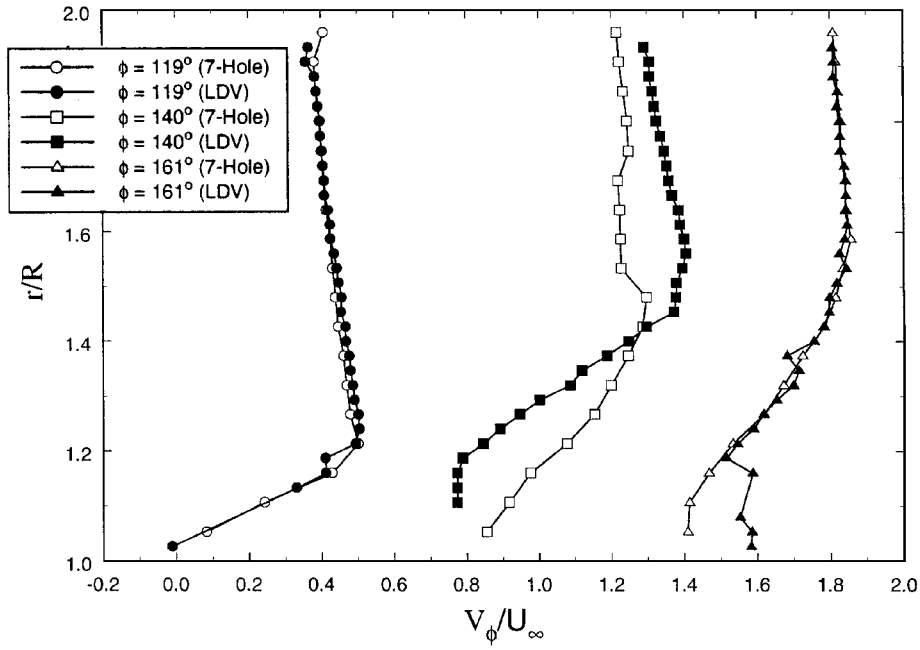

Fig. 12 LDV and seven-hole probe circumferential velocity profiles at $x/R = 9.7$, $\alpha = 20$ deg.

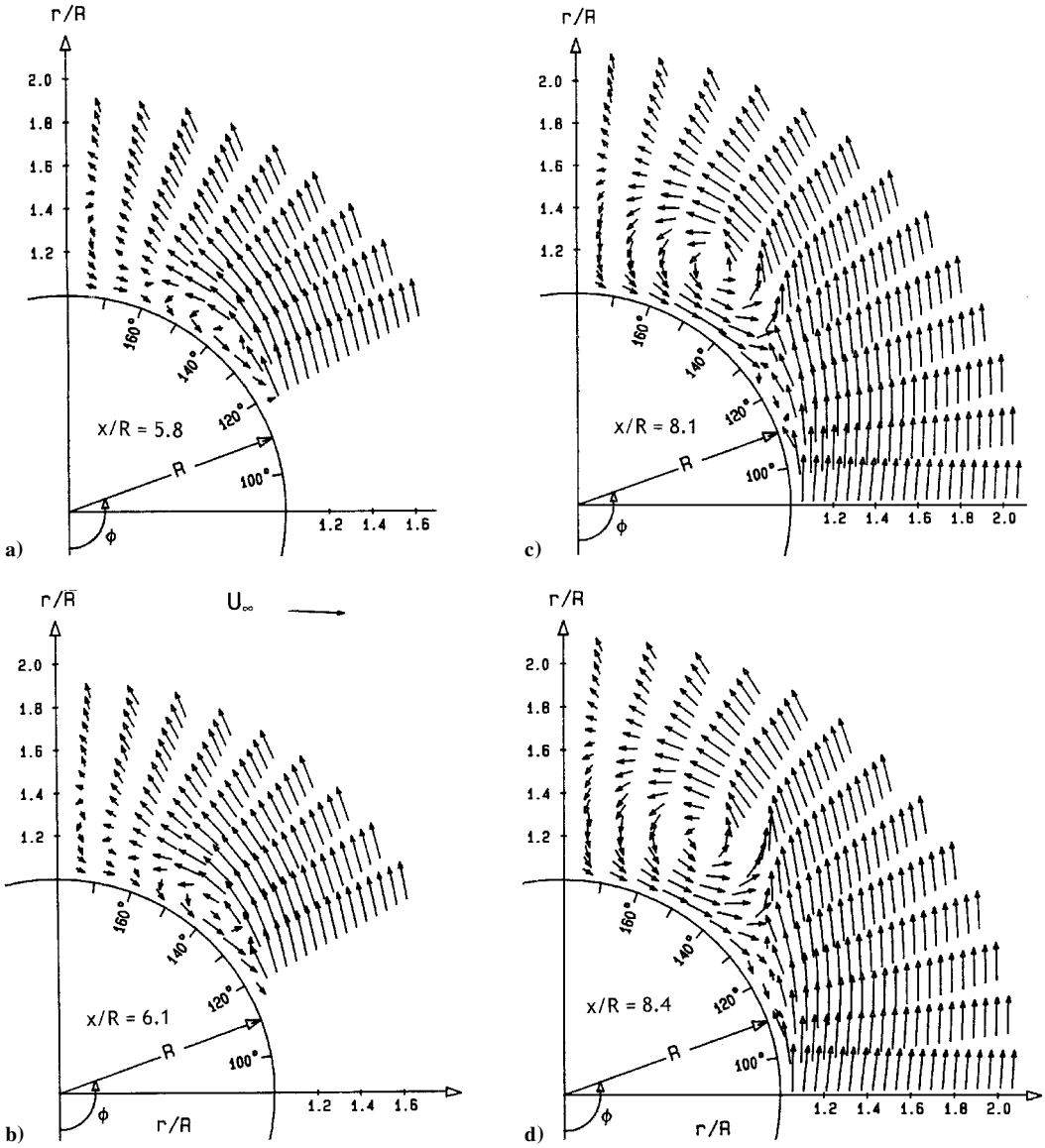

Fig. 13 Seven-hole probe velocity vector fields along a normal plane at $\alpha = 30$ deg, for $Re = 1.5 \times 10^5$.

probe. Moreover, the seven-hole probe has a much smaller spatial resolution than the fiber-optic LDV probe because its effective measuring volume is 4.5 mm, compared with 50 μm of the LDV probe.

Similar discrepancies between multiple-hole probes and LDV data for delta wing flows were also reported in Refs. 20 and 23. These authors reported deviations of LDV and five-hole probe data as high as 40% of each other for all three velocity components in the vicinity of high flow angularities and high velocity gradients, i.e., the vortex core. However, the two techniques agree well in regions of low shear and flow angularity.

Seven-hole probe data at stations $x/R = 5.8$, 6.1, 8.1, and 8.4 are presented in Fig. 13 for a Reynolds number of 1.5×10^5 and $\alpha = 30$ deg. At $x/R = 5.8$ and 6.1, the crossflow is strong, which causes the boundary layer to separate at about $\phi = 100$ deg. Figures 13a and 13b ($x/R = 5.8$ and 6.1) indicate recirculating flow in the domain $130 < \phi < 150$ deg. The vortical structure is not very well organized. Perhaps the flowfield is affected by the presence of the probe, because the size of the vortex at this station is still small. At $x/R = 8.1$ and 8.4 (Figs. 13c and 13d), both primary and secondary vortices are observed, and the primary vortex core locates near $\phi = 140$ deg. These vortices are much larger than those corresponding to the $\alpha = 20$ deg case. Again, a third vortex is not detected along the afterbody of the model at this angle of attack. At station $x/R = 5.8$, the agreement between the two methods outside the recirculating region is acceptable, as shown in Fig. 14. In this figure, constants of 1.0 and 1.6 were added to both LDV and seven-hole probe curves at $\phi = 160$ and 175 deg, respectively. The profiles of Fig. 14, for $\phi = 168$ and 175 deg, on the other hand, indicate a violent departure between the two methods of measurement in the vicinity of the vortex core. LDV data show much larger velocity values in the circumferential direction and, therefore, a much higher circulation in the vortex.

Figure 15 shows LDV data taken along $\phi = 160$ deg, $x/R = 8.1$, for $Re = 1.5 \times 10^5$ with the presence of the seven-hole probe. The probe was mounted at a fixed location, $r/R = 1.2$, $\phi = 160$ deg, $x/R = 8.15$. It would be more desirable to have the probe moving with the LDV measuring volume instead of keeping it fixed. However, this setup was not possible because there was only one

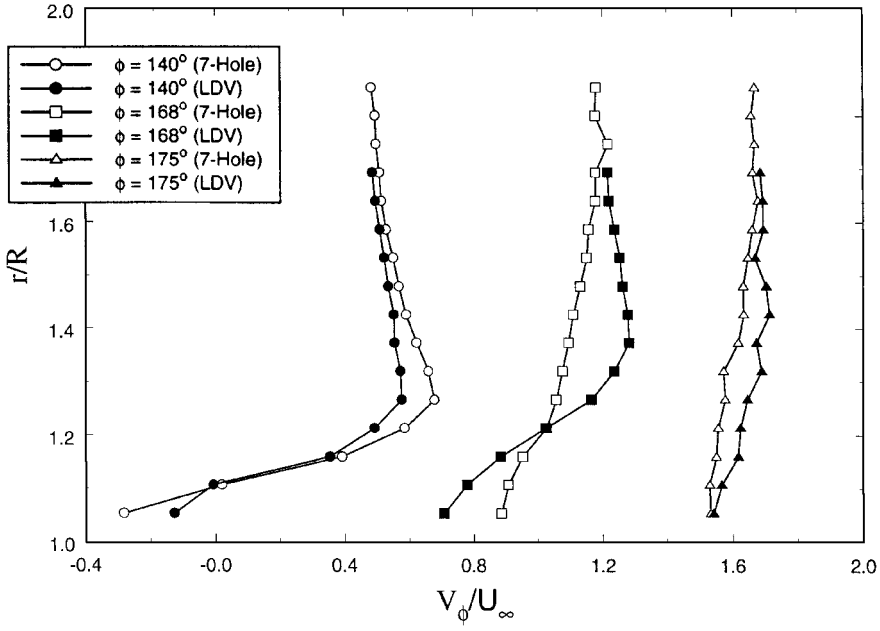

Fig. 14 LDV and seven-hole probe circumferential velocity profiles at $x/R = 5.8$ and $\alpha = 30$ deg.

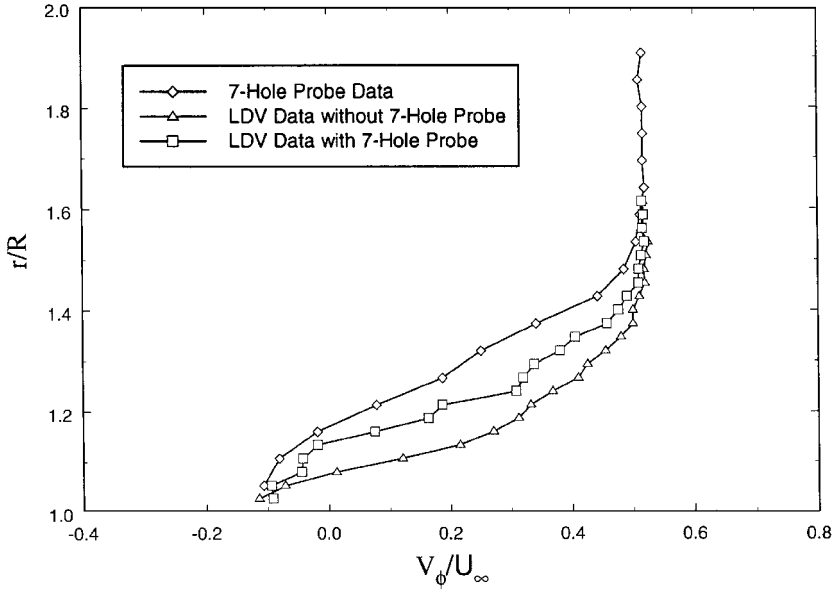

Fig. 15 LDV and seven-hole probe profiles at $x/R = 8.1$, $\phi = 160$ deg, $\alpha = 30$ deg, and $Re = 1.5 \times 10^5$ with added constants.

traversing mechanism available at the time. LDV data without the seven-hole probe and the seven-hole probe data obtained at the same location are also plotted in Fig. 15. LDV data obtained in the presence of the seven-hole probe consistently register values lower than LDV data obtained without the probe, and the seven-hole probe data register the lowest values at all locations inside the vortex. The results also show that the seven-hole probe has a global effect on the flow because the LDV data obtained in the presence of the seven-hole probe indicate that errors are not isolated to the neighborhood of the probe, but the effect is not significant if the seven-hole probe is not very near the core of a vortex or near the separation line.

Conclusions

For bluff axisymmetric bodies such as a hemisphere–cylinder at incidence, the flow around the nose develops very complex separation patterns. We have previously documented[18] the appearance of nose vortex rings and horn vortices in low Reynolds number flows. In the present paper we captured the range of moderate Reynolds numbers in which these patterns are modified and approach their high Reynolds number limit. We found that the separation bubble takes a form of a ring at low incidences but becomes an isolated bubble at higher incidences. Moreover, its width decreases as the Reynolds number increases. We also found that the nose structures are not connected with the separation lines that give rise to the vortical structures over the aft part of the body. Skin-friction patterns clearly indicate that regardless of the size and shape of the nose bubble, the flow develops open separation downstream. Superposition of skin-friction lines and pressure contours indicate that in the neighborhoods of bubble separation the pressure has troughs. The vortical structures emanate from the separation lines and grow with downstream distance. The results were documented digitally and are available to numerical analysts on request.

Comparison of LDV and seven-hole probe data indicates gross discrepancies in regions of high flow angularity, as in the core of vortices, or high velocity gradients, as in attached boundary layers approaching separation. We tend to trust the LDV measurements, even though it has been known that it is hard to seed the regions just mentioned. On the other hand, the seven-hole probe proved to provide quite accurate results away from these regions and, therefore, to capture the qualitative character of the vortices that develop over an axisymmetric body at incidence.

Acknowledgment

This work was supported by NASA Langley Research Center under Grant NAS1-18471, Stephen Robinson and William Sellers, Monitors. The financial and technical support of NASA and the collaboration of NASA personnel are appreciated. We are particularly indebted to Gregory S. Jones for arranging for the loan of the models, for his help in conducting liquid-crystal transition studies, and for many useful discussions and constructive criticism.

References

[1]Eichelbremmer, E. A., "Decollement Laminaire en Troid Dimensions sur un Obstacle Fini," ONERA, No. 90, Chatillon, France, Oct. 1957.

[2]Werlé, H., "Etude Experimentale au Tunnel Hydrodynamique de l'Ecoulement Autour d'une Familie d'Ellipsoides aux Faibles Vitesses," ONERA, NT 1/1859 A, Chatillon, France, July 1957.

[3]Wang, K. C., "Three-Dimensional Boundary Layer near the Plane of Symmetry of a Spheroid at Incidence," *Journal of Fluid Mechanics*, Vol. 43, Pt. 1, 1970, pp. 187–209.

[4]Maskell, E. C., "Flow Separation in Three Dimensions," Royal Aircraft Establishment, Rept. Aero 2565, London, Nov. 1955.

[5]Lighthill, M. J., "Introduction Boundary Layer Theory," *Laminar Boundary Layers*, edited by L. Rosenhead, Clarendon, Oxford, 1996, pp. 46–109.

[6]Wang, K. C., "Boundary Layers over a Blunt Body at Low Incidence with Circumferential Reversed Flow," *Journal of Fluid Mechanics*, Vol. 72, Pt. 1, 1975, pp. 49–65.

[7]Tobak, M., and Peake, D. J., "Topology of Two-Dimensional and Three-Dimensional Separated Flows," AIAA Paper 79-1480, July 1979.

[8]Tobak, M., and Peake, D. J., "Topology of Two-Dimensional Separated Flows," *Annual Review of Fluid Mechanics*, Vol. 14, 1982, pp. 61–85.

[9]Meade, A. J., and Schiff, L. B., "Experimental Study of Three-Dimensional Separated Flow Surrounding a Hemisphere–Cylinder at Incidence," AIAA Paper 87-2492, Aug. 1987.

[10]Meier, H. U., and Kreplin, H. P., "Experimental Investigations of Boundary Layer Transition and Separation on a Body of Revolution," *Zeitschrift für Flugwiss Weltraumforschung*, Vol. 4, Heft 2, 1980, pp. 65–71.

[11]Kreplin, H. P., Vollmers, H., and Meier, H. U., "Measurements of the Wall Shear Stress on an Inclined Prolate Spheroid," *Zeitschrift für Flugwiss Weltraumforschung*, Vol. 6, Heft 4, 1982, pp. 248–252.

[12]Barberis, D., and Molton, P., "Experimental Study of Three-Dimensional Separation on a Large Scale Model," *AIAA Journal*, Vol. 33, No. 11, 1995, pp. 2107–2113.

[13]Chesnakas, C. J., and Simpson, R. L., "Detailed Investigation of the Three-Dimensional Separation About a 6:1 Prolate Spheroid," *AIAA Journal*, Vol. 35, No. 6, 1997, pp. 990–999.

[14]Costis, C. A., and Telionis, D. P., "Unsteady Vortical Wakes over a Prolate Spheroid," *AIAA Journal*, Vol. 21, No. 8, 1983, pp. 1189–1193.

[15]Costis, C. E., Hoang, N. T., and Telionis, D. P., "Laminar Separating Flow over a Prolate Spheroid," *Journal of Aircraft*, Vol. 26, No. 9, 1989, pp. 810–816.

[16]Chesnakas, C. J., and Simpson, R. L., "Full Three-Dimensional Measurements of the Cross-Flow Separation Region of a 6:1 Prolate Spheroid," *Experiments in Fluids*, Vol. 17, No. 1/2, 1994, pp. 68–74.

[17]Hsieh, T., and Wang, K. C., "Three-Dimensional Separated Flow Structure over a Hemisphere–Cylinder," *Journal of Fluid Mechanics*, Vol. 324, 1996, pp. 83–108.

[18]Hoang, N. T., Rediniotis, O. K., and Telionis, D. P., "Symmetric and Asymmetric Separation Patterns over a Hemisphere Cylinder at Low Reynolds Numbers and High Incidences," *Journal of Fluids and Structures*, Vol. 11, Oct. 1997, pp. 793–817.

[19]Hoang, N. T., "The Hemisphere–Cylinder at an Angle of Attack," Ph.D. Dissertation, Dept. of Engineering Science and Mechanics, Virginia Polytechnic Inst. and State Univ., Blacksburg, VA, 1991.

[20]Rediniotis, O. K., Hoang, N. T., and Telionis, D. P., "Multi-Sensor Investigation of Delta Wing High-Alpha Aerodynamics," AIAA Paper 91-0735, Jan. 1991.

[21]Zilliac, G. G., "Modeling, Calibration, and Error Analysis of Seven-Hole Pressure Probes," *Experiments in Fluids*, Vol. 14, No. 1/2, 1993, pp. 104–120.

[22]Moffat, R. J., "Contributions to the Theory of Single-Sample Uncertainty Analysis," *Journal of Fluids Engineering*, Vol. 104, Sept. 1982, pp. 250–258.

[23]Klute, S. M., Rediniotis, O. K., and Telionis, D. P., "Flow Control over Delta Wings at High Angles of Attack," *AIAA Journal*, Vol. 34, No. 4, 1993, pp. 662–668.

J. C. Hermanson
Associate Editor